Journal of Material Science and Nanotechnology
Volume 14 | Issue 1
ISSN: 2348-9812

Research Article Open Access

Eco-firendly Adsorption of Reactive Yellow 84 from Wastewater Using Chicken Waste-Derived Ag-rGO Nanocomposite: A Comparative Study with GO and rGO

Flomo L Gbawoquiya[1*] Jutomue S Flomo[1] and Km Rachna[2]

[1]Department of Environmental Science, Cuttington University, Suakoko, Bong County, Liberia
[2]Deppartment of Environmental Sciences, Sharda School of Basic Sciences & Research, Sharda University, Greater Noida, India

Corresponding Author: Department of Environmental Science, Cuttington University, Suakoko, Bong County, Liberia E-mail: fgbawoquiya@cu.edu.lr

Citation: Gbawoquiya, F.L., Jutomue, F.S., and Rachna, K.M. (2026). Eco-friendly Adsorption of Reactive Yellow 84 from Wastewater Using Chicken Waste-Derived Ag-rGO Nanocomposite: A Comparative Study with GO and rGO. J Mater Sci Nanotechnol, 14(1), 103.

Received Date: July 15, 2026 **Accepted Date:** July 31, 2026 **Published Date:** August 06, 2026

Abstract

In this study, the comparative adsorption performance of biogenically produced silver-reduced graphene oxide nanocomposite (Ag-rGO NC) from discarded chicken waste (DCW) was evaluated against chemically synthesized graphene oxide (GO) and reduced graphene oxide (rGO) for the removal of Reactive Yellow (RY-84) dye from wastewater. Characterization of the adsorbents was carried out using X-ray diffraction (XRD), Fourier-transform infrared (FTIR), and Field-emission scanning electron microscopy (FESEM). Homogeneous dispersion of silver nanoparticles (Ag NPs) on rGO sheets was recorded at ~19 nm. Literature surveys have documented the use of GO, rGO, and Ag-rGO NC for dye adsorption; nevertheless, the adsorption performance of DCW-derived Ag-rGO NC in comparison to chemically synthesized GO and rGO of RY-84 dye adsorption remains underexplored. Following its application, Ag-rGO NC adsorbed 95% of the dye after 40 minutes of contact at pH 2 in contrast to GO and rGO, where 70% and 50% were recorded, respectively. From the thermodynamic studies, the process was spontaneous and exothermic. The maximum adsorption capacity was 70.58 mg/g, which was obtained from the Langmuir isotherm model. The Temkin isotherm model recorded a good fit ($R^2 = 0.998$) and recorded a decline in the heat of adsorption energy (BT = 12.28 J mol^{-1}), while the Freundlich isotherm showed a favorable capacity of adsorption at KF = 4.45 mg g^{-1} $(L/mg)^{1/n}$ occurring on a heterogeneous surface which was confirmed by the excellent fit ($R^2 > 0.99$). The NC retained its stability and recyclable characteristic, with 60% efficiency recorded after the fifth cycle of reuse. As such, the composite is effective against RY-84 compared to GO and rGO, making it an eco-friendly material.

Keywords: Chicken waste, adsorption, wastewater, Reactive yellow, nanocomposite

Introduction

The global shortage of safe drinking water arising from pollution is alarming. Because of the demand for safe and clean drinking water, the issue of pollution has been elevated to the level of a global crisis affecting water sources [1]. Various methods have been adopted in recent years to remove synthetic dyes, heavy metal ions, and microbial pollutants from water [2]. Different types of adsorbents have been carefully investigated for applications in wastewater treatment, including activated carbon [3], carbon nanotubes [4], metal organic frameworks [5], transition metal dichalcogenides, and varying polymers [6]. However, a large number of these adsorbents have shown limitations for an extended period of industrial-scale effectiveness in spite of their potential characteristics [7]. Amongst the different graphene derivatives, GO and rGO have been widely used due to ease of synthesis, large surface-to-volume ratio, good physicochemical properties, and extensive use across different fields [8]. Graphene possesses distinct mechanical, electrical, and thermal properties, making it a material of interest for many scientists with extensive use in the field of engineering [9]. When these graphene derivatives are incorporated with metallic nanoparticles such as silver (Ag) nanoparticles (NPs), zinc (Zn) NPs, Platinum (Pt), gold (Au), and copper (Cu), they produce nanocomposites (NCs) having multi-dimensions with improved ability for adsorption and antimicrobial functions. These versatile hybrid materials possess enhanced capabilities when used to treat wastewater [10, 11].

Silver (Ag) NPs, of the metallic NPs, have garnered immense attention because they possess excellent optical properties, effective chemical stability, and are easily compatible with biological systems. Ag-decorated NCs offer additional active sites for adsorption and help in electron transfer and accelerate interaction between contaminants and the surfaces of adsorbents, making them potential materials for wastewater treatment. Efficient treatment and reuse of wastewater are becoming essential because of the rise in global water pollution, which is attributed to the increased growth in human population [12]. Synthetic dyes originating from the textile industry are among key pollutants since they are highly soluble and their color persists much longer in water. Annually, a significant amount of azo dyes is released by different industries containing azo functional groups [13]. For instance, Nile blue (NB), mostly used as an azo dye, is known to be a hazardous compound with the potential of causing eye irritation, inflammation of the skin, allergic reactions, and diseases of the respiratory system (i.e., cancer). One major challenge that still remains is the treatment of industrial wastewater before discharge [14]. In recent times, however, different methods have been adopted to remove dyes from wastewater, ranging from coagulation, filtration, ultrafiltration, erosion, to adsorption and advanced oxidation [15]. Notwithstanding, the majority of these methods are cost-effective, and efficiency derived is quite minimal, which often produces secondary pollutants. Regardless of these challenges, adsorption is the most preferred option because of its cost-effectiveness, high efficiency, and ability to regenerate the adsorbent. Several materials have been employed as adsorbents with specific reference to activated carbon, porous polymers, zeolites, GO, ZnO, and silica. Metal-coated reduced graphene oxide composites like Pt/rGO, Au/rGO, Ag/rGO, Fe/rGO, and Pd/rGO have been preferred due to their synergistic adsorption performance, high selectivity, and extensive use [16].

For instance, the adsorption of naproxen from water using Ag-rGO NCs by Mondal et al. [17] achieved 92.62%, whereas methylene blue (MB) and Nile blue (NB) removal by Kamali et al. [18] using Fe–Al LDH-modified zeolite clay showed significant improvement. The use of other composites already reported in the literature has been effective in pollutant removal, such as MoO_3/Ppy composites for Cd^{2+} removal [19], CNT/MgO/$CuFe_2O_4$ NCs in methyl violet (MV) and NB remediation [20], and Ni–Co–S@Ct and hydroxyapatite Mn–Fe for MB, crystal violet (CV), NB, Congo red (CR), dyes, and toxic metal ions such as As(III) and As(V) adsorption [21-23]. Elsewhere, it has also been reported that the use of Ni–Co–S/SDS composites recorded the removal efficacy of NB dye at 95% [24], while heterostructure materials like Fe_3O_4/rGO and Fe_3O_4/MoS_2/rGO showed great prospects for nitroanilines remediation from water [25]. A recent study on the use of green-synthesized nanocomposites (ZnO-rGO) showed high removal efficiency for rhodamine B (RhB) and basic fuchsin (BF) dyes, respectively, as well as chitosan–MgO and polypyrrole–TiO_2 (Ppy/TiO_2) for heavy metal removal [28, 29].

As research expands, different materials have been tested and used extensively in the formation of composites as reducing and stabilizing agents. Among those materials are agriculture and food wastes used as reducing and stabilizing agents because they contain proteins, carbohydrates, and other essential biological molecules capable of reducing metal ions into stable NPs. These molecules are capable of addressing the hurdles related to the effective management of waste and aiding the production of nanomaterials that are eco-friendly. While there has been progress, few studies exist on producing these materials in a circular economy. Of all the biomass wastes, DCW is one of the least studied types in the field of materials science. DCW remains one of the least studied biomass wastes in the field of materials science. These wastes contain proteins and metallothionein-like compounds that serve as reducing and stabilizing agents naturally whenever NPs are synthesized.

While advancements in the production and use of graphene materials remain an integral part of material science and nanotechnology for the remediation of harmful dyes and metal ions, there is a gap in understanding the mechanistic and comparative adsorption behaviors of chemically produced GO and rGO, as well as biogenically produced Ag NPs decorated on rGO for RY-84 dye removal from water. The literature survey revealed abundant materials on chemically graphene-based materials coated with metallic NPs without the use of chemical and green methods of synthesis in the context of a comparative framework. In spite of the fact that reducing agents from biological wastes have been researched for the production of NPs, the use of DCW, which contains a thiol and protein-rich biological molecules with metallothionein as reducing and stabilizing agents in synthesizing Ag-rGO NC, has not been reported in the literature. Likewise, among parameters that are underreported are pH, contact time, dose, and dye concentration with isothermal and kinetic analysis. As a result, there is a lack of scientific clarity on the synthesis processes of Ag-rGO composites using DCW and their effectiveness in adsorption studies compared to GO. To bridge this gap would be essential for the future development of eco-friendly graphene-based composites and their use in water purification systems for dye pollutants.

Materials and Methods

All chemicals and reagents used are analytical grade. These include silver nitrate ($AgNO_3$, 99% purity, Sigma-Aldrich), sodium nitrate ($NaNO_3$, 99.99% purity, Fisher Scientific), sulfuric acid (H_2SO_4, 98% purity, Somadi), hydrogen peroxide (H_2O_2, 30% w/v, Somadi), acetone ($(CH_3)_2CO$, Somadi), hydrochloric acid (HCl, Somadi), potassium permanganate ($KMnO_4$, 98.5% purity, Fisher Scientific), and sodium hydroxide (NaOH, 99%). All chemicals and reagents used are analytical grade. These include silver nitrate ($AgNO_3$, 99% purity, Sigma-Aldrich), sodium nitrate ($NaNO_3$, 99.99% purity, Fisher Scientific), sulfuric acid (H_2SO_4, 98% purity, Somadi), hydrogen peroxide (H_2O_2, 30% w/v, Somadi), acetone ($(CH_3)_2CO$, Somadi), hydrochloric acid (HCl, Somadi), potassium permanganate ($KMnO_4$, 98.5% purity, Fisher Scientific), sodium hydroxide (NaOH, 99% purity, Fisher Scientific), and thiourea (NH_2CSNH_2). % purity, Fisher Scientific, and thiourea (NH_2CSNH_2) were used.

Discarded Chicken Waste (DCW) Preparation

The DCW broth was extracted using the modified method employed in previous studies [30]. About 200 g of chicken intestine was procured from the local market, properly cleansed, and rinsed thrice using distilled water to get rid of blood stains and other impurities. The cleansed tissues were placed in 200 mL of 50% ethanol and kept safely at 50 ± 5 °C for the duration of 10 minutes under mild heat. The Whiteman #1 filter was used to filter the solution in order to extract the ethanolic extract. The residual tissue was boiled in 200 mL of distilled water for 10 minutes to remove any available metabolites. The aqueous extract obtained was carefully filtered. The ethanolic broth and aqueous extract were combined. The resultant solution, with immense biological molecules, was used as reducing and stabilizing agents for the synthesis of NPs.

2.2 Silver Nanoparticles (Ag NPs) Synthesis

The prepared DCW solution was combined with 0.25 M (20 mL) solution of silver nitrate and subjected to continuously stir-

ring at 60 °C for 10 minutes to speed up the reduction of Ag^+ ion. At room 25 °C, the mixed solution was cooled and store in the lab followed by a change in color from pale yellow to reddish brown indicating that silver nanoparticle was formed. After about 5 minutes of starting the reaction, a deposition was visible. The mixture was kept for 5 hours to ensure the complete formation of NPs. It was later filtered, and the filtrate was suspended in distilled water and centrifuged at 10,000 rpm for 20 min to extract biological molecules that failed to react. The pellets were dried in a hot air oven.

Synthesis of graphene oxide (GO) and reduced graphene oxide (rGO)

The synthesis of GO followed the Hummers' method [31]. Graphite powder (3 g), 1.5 g of sodium nitrate ($NaNO_3$), and 115 mL of concentrated sulfuric acid (H_2SO_4) were combined in an ice bath for 20 minutes. 9 g of potassium permanganate ($KMnO_4$) was slowly added to the mixture and stirred repeatedly to regulate temperature above 20°C and prevent excessive oxidation. The reaction lasted for 12 hours while the temperature was slowly increased to 35 °C. The mixture was further heated to 98°C with the addition of 300 mL of distilled water carefully to avoid thermal escape. The final volume of the suspension was increased to 1 liter of distilled water, and the residual manganese species was removed by adding 30% hydrogen peroxide (H_2O_2) until the solution's color was changed, indicating the completion of the oxidation process. The resultant mixture was washed and filtered with 5% hydrochloric acid (HCl) and distilled water to achieve a neutral pH. The purified GO was vacuum-dried for 24 hours to obtain a solid product. The rGO was produced by dispersing it in a thiourea solution as a reducing agent (Fig. 1). The mixture was continuously stirred at a constant temperature of 100°C for 24 hours. These chemical and thermal processes enhanced the conversion of GO to rGO consistent with the synthesis method already reported [32].

Figure 1. Schematic depiction of GO and rGO synthesis using modified Hummer's Method

Synthesis of Ag-rGO nanocomposite

The synthesis of Ag-rGO NCs was done using sonicated-assisted method to ensure homogenous dispersion and strong interfacial interaction between Ag NPs and the rGO sheets. 0.1 g of rGO and 0. 25 g of Ag NPs were separately dispersed into 100 mL and 50 mL of distilled water respectively using ultrasonic bath (40 kHz, 200 W) for 30 minutes each under continuous stirring. The both mixtures were later combined and sonicated for additional 45 minutes under continuously stirring to facilitate the anchoring of Ag NPs on rGO surface homogeneously. 0.45 μm membranes were used to filter the final mixture which was washed severally with ethanol and distilled water and vacuum-dried at 60°C for 12 hours.

Preparation of Reactive Yellow (RY) Dye

A stock solution of RY-84 dye of 100 mg/L was prepared. 100 mg of RY-84 dye powder was placed in 1 L of distilled water and stirred constantly to allow proper dissolution. Working solutions of 10, 20, 30, and 40 mg/L were prepared from the stock solu-

tion via serial dilution. The solutions were stored in amber bottles to avoid photo gradation of the dye's solution which were later used for the experiment.

Batch Adsorption Experiment

A UV-visible spectrophotometer was used to analyze the removal efficiency of the dye. The maximum adsorption wavelength (λmax) was recorded at 263 nm. The synthesized adsorbents (GO, rGO, and Ag-rGO NC) were used to study various parameters such as contact time (0 – 40 mins.), adsorbent doses (0.05 – 0.20 g), initial dye concentrations (10 – 40 mg/L), and pH (2 – 10). 0.1 N NaOH and 0.1 N HCl were used for pH adjustment for every solution. In equation 1, the percent removal (%R) of the dye was computed.

$$\%R = \frac{(Co - Ce) \times 100}{Co} \quad (1)$$

The initial dye concentration C0, was determined in mg/L, while Ce denotes the equilibrium dye concentration remaining in the solution after adsorption (Eq. 2).

$$q_e = \frac{(Co - Ce)\, V}{m} \quad (2)$$

In Equation 3, the adsorption capacity of RY-84 dye onto Ag–rGO NC adsorbent is expressed in milligrams per gram (mg/g). Here, C0 denotes the initial dye concentration (mg/L), Ce is the equilibrium dye concentration (mg/L), V represents the volume of the dye solution in liters (L), and W indicates the mass of the adsorbent used in grams (g).

$$q_t = \frac{(Co - Ce)\, V}{W} \quad (3)$$

Results and Discussion

X-ray diffraction analysis of GO, rGO, and Ag-rGO NC

The oxidation of graphite was done successfully, as indicated by the XRD patterns in Figure 2. Notable diffraction peaks appeared around ~2θ = 10-12° of GO, which correspond to the (001) plane. During oxidation, oxygen-containing functional groups facilitated the emergence of the existing peak. The interlayer spacing of the GO was triggered by oxygen functionalities and intercalation of water molecules from 0.34 nm to 0.80–0.90 nm, respectively [33, 34]. The visibility of the graphitic digression of (002) at 26° as well as the GO (001) peak resulted from the exfoliated arrangement in the morphology of the GO, which is typical of GO materials and has already been reported [35]. The emergence of a peak between 10° and 12° indicates that following oxidation, the hydrophilic graphene sheets experienced structural imbalance because when the (001) peak appeared, graphite layers underwent significant oxidation [36, 37]. By its very nature, purified graphite usually has a sharp peak around (002), which is about 26.5°. In this study, however, the crystal structure of GO experienced an increment but with a lower peak, affirming the addition of oxygen. When GO experiences an extension in its peak, it is indicative that its crystal nature is reduced, leading to its structural instability [38].

Unlike GO, rGO displayed a significant change in its morphology (Fig. 2). From all indications, the GO (001) peak literally disappeared following the reduction process and was suddenly replaced with a broader peak around 24-26°, which corresponds to the (002) carbon plane of graphite. A carbon framework that is partially hybridized is being restored while the disappearance of oxygen functions containing carbon remains quite visible. Graphene sheets are capable of reassembling once the arrangement/order is less so as opposed to graphite due to interlayer gap reduction, which usually appears because of the extraction of oxygen functionalities. When a broad peak (002) appeared, it signaled the extent to which oxygen functions or impurities existed in the material, resulting in the incomplete nature of the graphitization process. This phenomenon is often observed when GO

is being reduced to rGO [37, 39]. While the reduction of GO to rGO ensures that the rGO remains electrically conductive, rGO does not lose structural integrity from pristine graphite. This is because there are no alterations that exist within the rGO [40]. The displacement of the peak is improperly arranged towards the direction of higher angles; it indicates success in the reduction process and a homogenous sequence in the architecture of the graphene sheets.

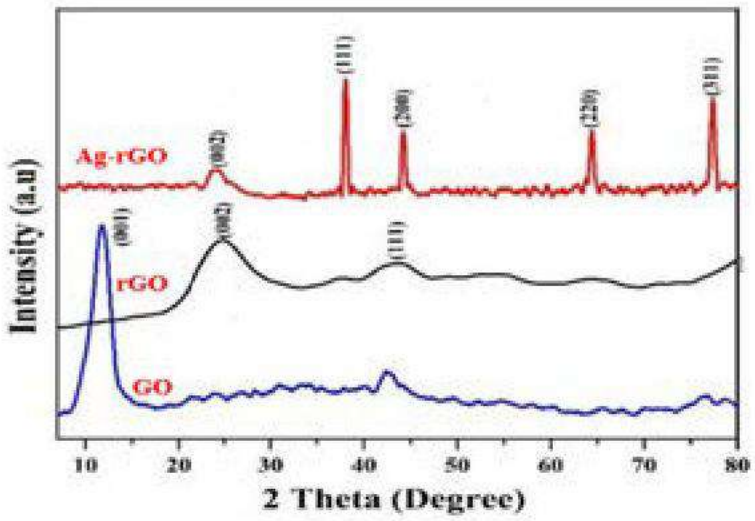

Figure 2. XRD spectra of GO, rGO, and Ag-rGO nanocomposite

The nanocomposite displays various diffraction peaks at about 38°, 44°, 64°, and 77°, which align with (111), (200), (220), and (311) planes, respectively (Figure 2). The Ag^+ ions in this case were effectively converted to more crystalline metallic Ag^+ NPs situated on the surface of the rGO. At peak (111), the orientation of the crystal Ag NPs is ideal because it reflects standard surface energy and a high thermodynamic stability of face-centered cubic (FCC) planes of silver. No peaks directly related to silver oxides can be seen, which confirmed the purity of Ag NPs. However, the presence of the (002) peak remains apparent, suggesting the indestructible framework of graphene following the deposition of NPs. Similar diffraction peaks have been observed and attributed to the FCC morphology of metallic silver coupled with the deposition of similar Ag NPs on highly crystalline sheets of graphene. When silver NPs lack impurities, it usually reflects the absolute reduction of metallic silver void of oxide components [41-43]. The aggregation of the NPs can be prevented by rGO with the provision of nucleation and stabilization sites, which yield NP development [44]. When compared to rGO, the presence of peaks in the NC suggests that the crystalline nature of the nanoparticles was significantly high but maintained the structure of the graphene. The average crystallite size of the NC for this study was determined using the Debye–Scherrer equation (Eq. 4) [45]:

$$D = \frac{K\lambda}{\beta COS\theta} \quad (4)$$

Where, D represents the crystallite size of the composite, K is the shape factor (commonly taken as 0.94), λ denotes the wavelength of the X-ray source, β corresponds to the full width at half maximum (FWHM) of the diffraction peak (in radians), and θ is the Bragg angle. The crystallite size of the NC was found to be approximately 19 nm.

FE-SEM analysis of GO, rGO, Ag-rGO NC

Silver nanoparticles (Ag NPs) are predominantly spherical with a uniformed shape and distributed evenly (Fig. 3a). Most of the particles exhibit varying nanoscale sizes; however, there is a little degree of aggregation visible in select areas due to the high surface energy on their surface. The aggregation of individual NPs appeared orderly during the synthesis procedure, aiding in the reduction of free energy on the particle's surface via interaction through the van de Waals force. Notwithstanding, effective

growth and nucleation are observed from the NPs due to the dispersion signal, though the signal appears to be a bit narrow in size. The use of green methods for Ag NP production has often resulted in a more spherical architecture in terms of the particle size depending on the type of agents used for reduction [46]. The interactions that exist between particles are due to the uniform dispersion of the spherical NPs with less clustering. It is most likely for NPs to always cluster since the energy associated with their surface area is always high, which is one key attribute for the particles of silver [47]. Regardless of the clustering detected in Ag NPs for this study, there is no alteration in the large surface area and active sites, which is essential for their adsorption behaviors. When compared to bulk silver, nevertheless, the structure helps with the improvement of the surface reactivity, which facilitates interaction with the dye molecule. With the homogenous dispersion of the NPs, we can confirm that an ideal nucleation during synthesis occurred, which implies that the growth of the particles is controlled by the reducing agent [48].

GO exhibits structured layers with a sheet-like appearance ideally arranged, curled and folded (Fig. 3b). The exfoliation on the GO surface is quite essential, indicated by the uneven edges containing multiple layers that are interwoven, reflecting the fundamental changes during the oxidation process. Quite often, the wrinkling and folding seen on the GO surface are typical features associated with GO which originate from the addition of oxygen functionalities, causing disruption in the lattice plane of graphene, leading to an increase in its rough surface and intermittently inhibiting the reaggregation of graphene sheets. These unique features have been associated with numerous findings in contrast to pristine graphite, which possesses surface roughness and porosity [34, 36; 49].

The thickness of the graphene sheet is significantly reduced in Figure 3c, which further results in reduced density and increased exfoliation. This results in a silk-like, translucent shape and causes a decline in the stacked layers. When graphene sheets are reduced, a large portion of oxygen-containing functional groups are removed, causing the graphitic carbon networks to slightly re-establish themselves and subsequently encounter varying structural imperfections and pores within the sheets. The wrinkled appearance is retained but not easily seen compared to GO, which implies that the reduction process was successful and, at the same time, the interwoven graphene architecture was slightly restored. When chemically reduced, highly oxidised rGO sheets become much thinner and flexible, with the graphene layers having less interlayer spacing because oxygen functionalities in this case are significantly reduced, resulting in this structural defect [37, 39, 50]. These thin and flexible layers help in the enhancement of adsorption efficacy, for they increase the number of active sites for the remediation of adsorbate. In addition, the restoration of the sp^2 carbon architecture enhanced the π-electron density, which invigorates pi-pi interaction between graphene and the dye's molecules [36, 51]. In Figure 3d, the nanocomposite displays successful anchoring of Ag NPs on the surface of the graphene material. The multi-layered and wrinkled rGO sheet is homogeneously decorated with several visible Ag NPs, indicating an effective interaction between the NPs and oxygen functions on the rGO surface. The inhibition of the wrinkled rGO sheets is accompanied by intense restacking of the graphene layers and provides large surface area and more active sites to have the NPs deposited.

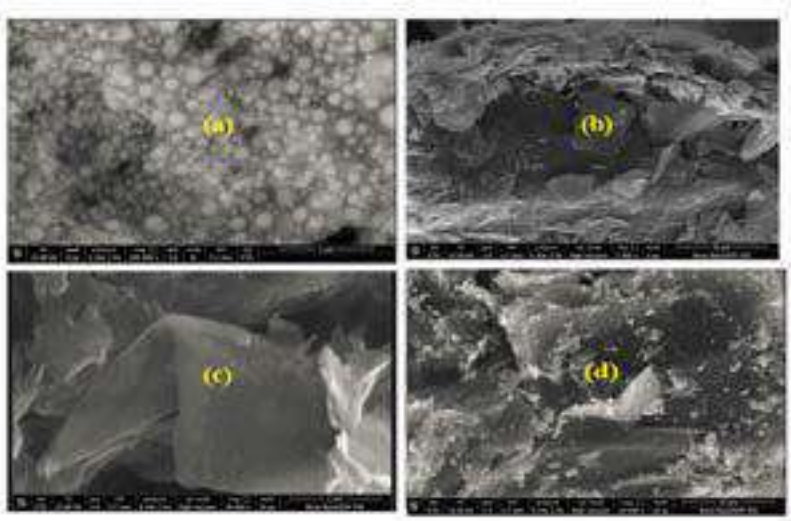

Figure 3. FE-SEM images of synthesized materials for RY-84 removal (a) Ag NPs, (b) GO, (c) rGO and (d) Ag-rGO NC

UV-visible Spectra of GO, rGO, and Ag-rGO NC

The UV-visible spectra of the adsorbents are given in (Figure 4). A gradual change in the architecture and optical properties of the materials exists. GO spectrum (blue curve) exhibits a remarkable adsorption peak around 230 nm. The occurrence of this peak is due to the electronic migration of the π–π interaction of aromatic C=C bonds in the hybridized domains. During GO synthesis, oxidation produced an electronic transition associated with C = O bonds, which is represented around 300 nm on another shoulder. These distinctive features pinpoint the level of extreme oxidation of the carbon framework and the incorporation of oxygen functionalities. A notable shift in the adsorption peak is observed at about 270 nm following the chemical reduction of GO to rGO (black curve) [52]. At 300 nm, a reduced shoulder appeared, indicating the recovery of the conjugated pi--electron framework and oxygen-containing functional group removal. The alteration in the spectrum facilitates the delocalized nature of rGO by further supporting the reduction and re-introduction of pi-pi interactions within the graphitic lattice. Furthermore, the composite's spectrum (red curve) retains its usual peak about 270 nm. This retention further supports structural stability that exists within the matrix of rGO following the deposition of the Ag NPs, while larger adsorption bands at 350 – 450 nm resulting from the surface plasma resonance (SPR) subsequently appeared [53]. The band from the SPR usually arises when floating electrons in the NPs uniformly oscillate where the particles are subjected to light, which explains the rationale behind the smooth anchoring of Ag on the surface of rGO.

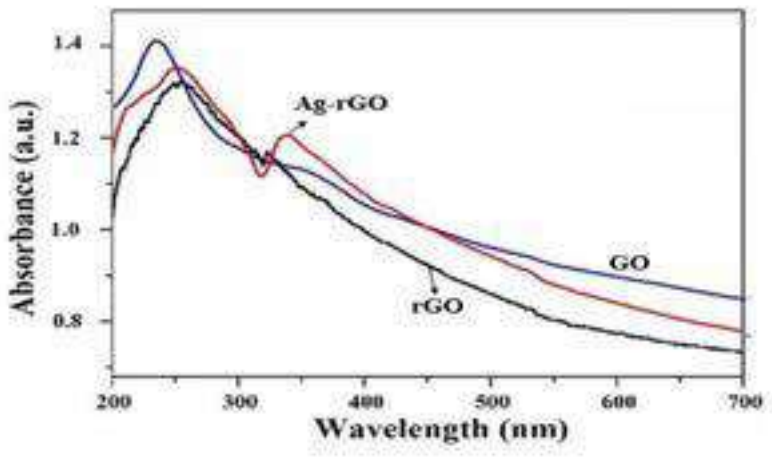

Figure 4. UV-visible adsorption spectra of GO, rGO, and Ag-rGO NC.

FTIR analysis of GO, rGO, and Ag-rGO NC

Essential information on functional groups on the composite's surface for RY-84 dye remediation is given in Figure 5. Gradual alterations are observed, affirming the successful oxidation of the GO and subsequent reduction to rGO before the Ag-rGO NC was produced. When the surface of the adsorbents is altered with specific reference to their surface chemistry, active sites, and interaction with the dye molecule, this morphological enhancement impacts the adsorption performance of the adsorbents.

Different features of adsorption bands linked to oxygen functional groups emerge during the oxidation of graphite. There are notable hydroxyl (OH) groups causing the stretching vibration along with molecules responsible for the broad band around 3411 cm^{-1}, indicating the hydrophilic nature of the materials. The asymmetric stretching vibration of aliphatic C–H bonds is also observed at 2923 cm^{-1}, while the adsorption band causing the carbonyl (C =O) groups to vibrate is derived from carboxylic acid oxygen functionalities derived from ketones and is associated with a notable peak at 1725 cm^{-1}. During graphite's oxidation and the synthesis of GO, an adsorption band was produced near 1055 cm^{-1}, which was accompanied by the distorted vibration of C–OH groups situated at 1383 cm^{-1}. These findings are consistent with the production of graphene oxide using the Hummers' method, where the spectra in similar syntheses were found to be 3400 cm^{-1}, 1720 cm^{-1}, and 1050 cm^{-1}, respectively [34].

In contrast to GO, rGO experienced significant alteration, which implies that the reduction method was effective. Near 3411 cm^{-1}, a large band of adsorption can be seen, but the intensity decreased significantly, which suggests that some of the hydroxyl groups were eliminated during reduction. Similarly, the carbonyl peak exhibits a notable feature at 1725 cm^{-1} but appears completely diminished, implying that the carbonyl functional groups were effectively removed. Importantly, 1574 cm^{-1} and 1249 cm^{-1} adsorption bands exist, but their presence is attributed to the skeletal vibration of the aromatic sp^2 C=C bonds resulting in the restoration of the structural framework of graphitic carbon after the reduction procedure. A weakened epoxy vibration emerged in the rGO, unlike GO, implying that most of the oxygen functions were already being removed. Nevertheless, small fragments were retained on the graphene's surface, a scenario that has previously been reported [37].

The FTIR spectrum of the nanocomposite possesses unique features that are characteristic of rGO, but the intensity of a notable peak shifts slightly upon Ag NP addition and quickly reduces (Figure 5). There is a broad hydroxyl band at 3411 cm^{-1} but with reduced intensity, although it is still visible. This suggests the availability of a small amount of -OH groups on the surface of graphene. An aromatic framework is seen at 1574 cm^{-1} due to the retention of the graphene structure upon the deposition of the NPs. Furthermore, at 1249 cm^{-1}, an adsorption band linked to epoxy was retained but with less intensity when compared to GO. The anchoring of Ag NPs on the surface of graphene was effective due to the addition of the remaining oxygen functions, and since there are no new adsorption bands clearly visible, the NPs uniquely interacted with the oxygen functionalities via coordination instead of creating new covalent bonds [41, 42]. The majority of the oxygen functional groups were eliminated during reduction, leading to the restoration of the sp2 carbon framework of rGO; however, oxygen residuals were produced and served as nucleation sites for Ag NPs, which resulted in the homogeneous coating of the particles in the rGO matrix [51].

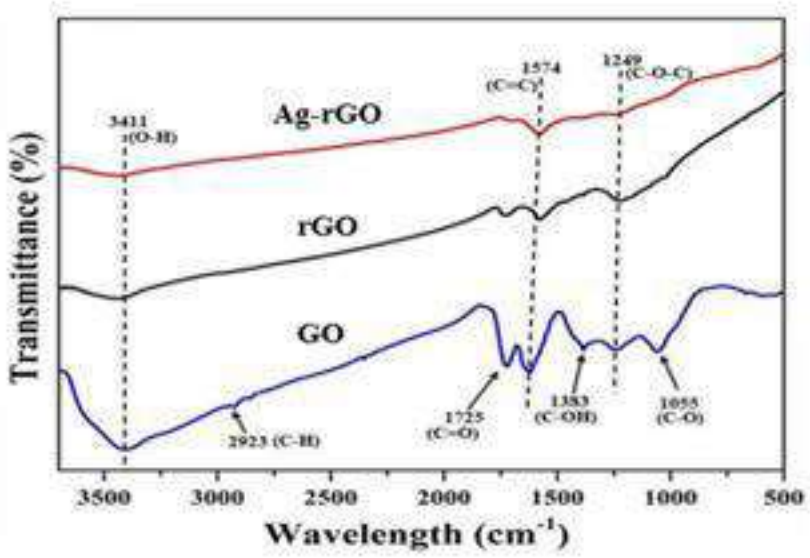

Figure 5. FTIR spectra of of adsorbents for RY-84 dye removal GO, rGO, and Ag-rGO NC

Raman spectra of rGO and Ag-rGO nanocomposite

Two distinct spectra corresponding to D and G bands for rGO and the NC are presented in Figure 6 with different positions: 1350 cm^{-1} and 1580-1600 cm^{-1}. The presence of structural impurities and disorders within the carbon structure is represented by the D band, followed by an in-plane vibration of sp^2 carbon atoms bonded within the graphite structure, represented by the G band. The rGO spectrum (black curve) exhibits the two peaks signaling that the reduction of GO was done partially as well as the reestablishment of the graphene architecture, although there is a perceived defect in the material. The composite (blue curve) indicates a remarkable increase in both the intensity of the D and G bands. This increased intensity is linked to the surface-enhanced Raman scattering (SERS) effect caused by the NPs [55]. This implies an electronic interaction and charge transfer occurring between the NPs and rGO sheets, culminating in increased defect sites and improved conductivity. The differences in the spectra confirm the anchoring of the NPs on the surface of the rGO, producing the composite with enhanced optical and structural features [56].

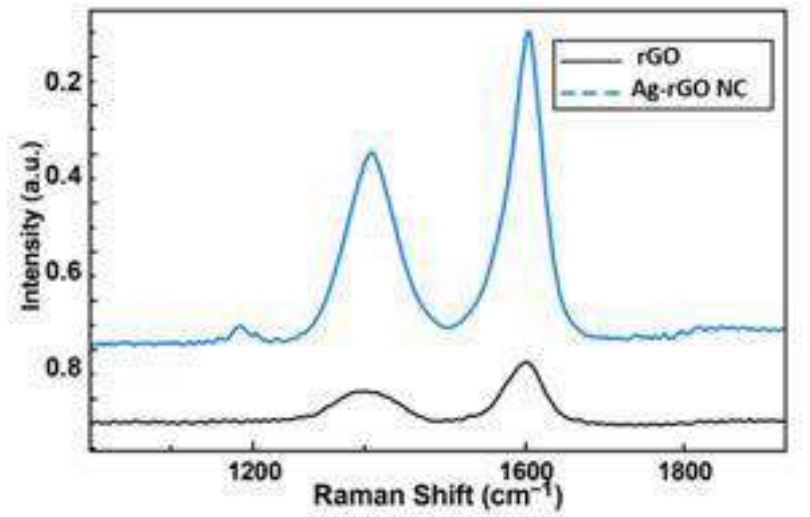

Figure 6. Raman spectra of rGO, and Ag–rGO nanocomposite

Adsorption of RY-84 Dye under different Conditions

Effect of Contact Time

The adsorption of RY-84 was assessed as a funtion of time. The nanocomposite recorded the highest percent removal (%R) at 95% in 40 minutes, while the GO and rGO recorded a removal efficiency of 70% and 50%, respectively (Figure 7). A similar trend has also been reported on the effectiveness of nanocomposites with high %R recorded across various systems of dye removal. The high %R observed by the composite is due to the synergistic impact of the rGO matrix increasing the surface area of the material, leading to the interaction between pi bonds. These interactions provide more active sites for the remediation of the dye molecules. The %R of the rGO is quite moderate because the pie-conjugated framework was restored and the surface area of the material was slightly recovered. The low performance of GO is influenced by the presence of oxygen functional groups, which prohibit pi-pi aggregation, coupled with the reduction in adsorption sites. The adsorption mechanism shows a unique kinetic behavior of the materials dominated by initial dye uptake subsequently followed by a plateau as the sites on the surface of the adsorbent gradually saturate. This observation implies that the adsorption sites became limited, serving as the governing mechanism. Therefore, the results confirmed the important role associated with the surface modification and the decoration of NPs to optimize graphene-based adsorbents, offering a pathway to design materials with high removal efficacy for dye removal.

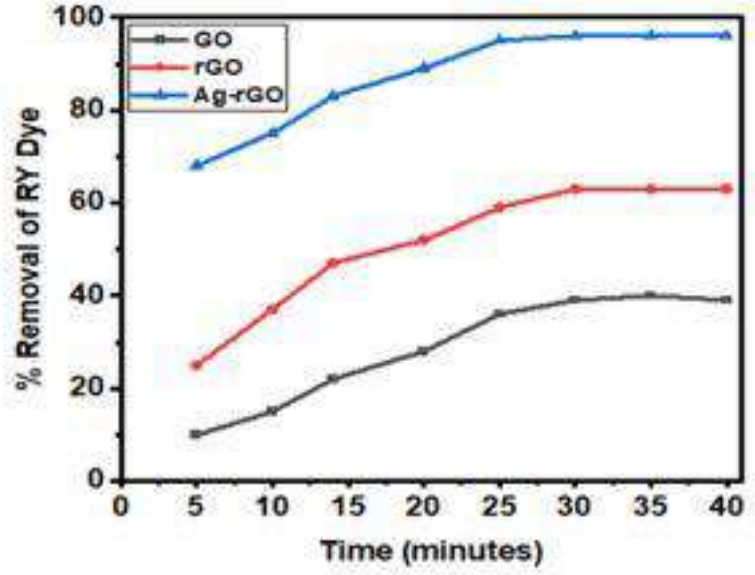

Figure 7. Effect of Contact Time of %R of RY-84 Dye on GO, rGO, and Ag-rGO NC. Dose = 0.20g/L; Conc. = 20mg/L (20 mL volume); and pH =2.

Effect of Initial Concentrations

The influence of the initial RY-84 dye concentration using Ag-rGO NC was studied. The findings show a unique but inverse relationship between the dye concentration and the effectiveness of the adsorbent consistent with those already reported. The lowest concentration (i.e., 10 mg/L) recorded the highest %R due to the availability of more active adsorption sites on the surface of the composite relative to the amount of RY-84 dye molecules in the solution. In addition, the surface of the adsorbent was far from being saturated, leading to more cohesive electrostatic and pie-pie interactions between the RY-84 molecules and the composite's surface. When the dye's initial concentration was increased to 40 mg/L, the %R dropped remarkably to 57%. This decline is apparently due to the gradual occupation and subsequent saturation of the active sites available. Saturation of active sites prohibits the remaining molecules of RY-84 from being adsorbed, leading to an overall decline in the %R (Figure 8a). In

similar studies, the %R also declined from 99% to 48% when the initial concentration of dye increased from 5 mg/L to 60 mg/L; the authors alluded to sites' saturation and stacking of dye molecules, increased dye loading, and limited number of active sites, which hinder the removal effectiveness [48, 58]. This study demonstrates the crucial relationship between key parameters such as the initial concentration, availability of surface sites, and the dynamism associated with mass transfer during adsorption. More active sites are available on the adsorbent's surface when dye concentrations are lower, yielding maximum uptake and high %R. On the contrary, an increase in the concentration creates a unique competition between dye molecules for access to limited active sites. During this period, the competition is intense, and aggregation of molecules may occur and reduce accessibility to efficient surface area for adsorption and subsequent diffusion in the composite's matrix. Therefore, while the potential of the composite during dye adsorption at low concentrations is excellent, its ability to adsorb dye molecules at high concentrations decreased, stressing the importance of the optimization of operational parameters during adsorption studies.

Effect of Adsorbent Dose

Different adsorbent doses (0.05 g/L to 0.20 g/L) of Ag-rGO NC were evaluated for RY-84 dye removal. A correlation exists between Ag-rGO NC and %R. The %R at lower doses declines because of the limited number of active sites for dye removal. During this period, there are relatively fewer particles to trap RY-84 dye molecules, resulting in the high possibility of saturated sites and low %R. When the adsorbent dose is increased, however, the %R improved significantly, indicating that most of the RY-84 molecules present in the solution were adsorbed. This phenomenon is consistent with the theory of adsorption, which predicts that more adsorbent doses yield a large surface area and active sites for effective interaction with adsorbate molecules, which has been reported in similar studies for reactive red 120 dye and methylene blue for composite materials [59, 60, 1]. The positive relationship observed in this study between Ag-rGO NC and RY-84 in regard to %R highlights the importance of the availability of more active sites in batch adsorption studies while prioritizing the optimization of adsorbent dose to improve adsorption performance in practical wastewater treatment scenarios.

Effect of pH

The effect of pH on RY-84 dye was studied, and results are presented in Figure 8c. An inverse relationship was observed when the pH ranges from 2 to 10 were studied. An increase in the pH was noticeable with 90% removal efficiency recorded at pH 2, but a further increase in the pH from 4 to 6 resulted in a gradual decline, although the %R remains relatively high. Between pH 6 and 8, there was a decline in the %R, and above pH 8 there was no significant variation in the %R, which appeared relatively consistent but with the lowest %R. This inverse relationship is attributed to the charge on the surface of the composite and the ionization state of RY-84 dye molecules. The surface charge of the Ag-rGO NC adsorbent may have been positively charged in an acidic medium, a condition that necessitated the electrostatic attraction of the negatively charged molecules of RY-84 dye. As the pH increased, the electrostatic repulsion and a decline in the %R were due to the less positive nature or negative charge. Hence, making pH 2 the ideal acidic environment for RY-84 dye removal.

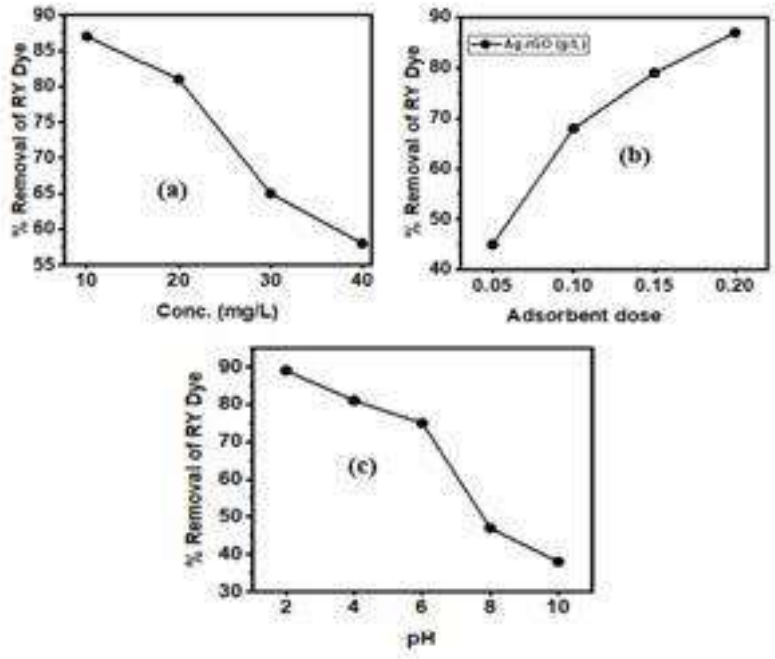

Figure 8. Percent removal of RY-84 dye uner different conditions, (a) dye concentration, (b) adsorbent dose, (c) pH.

Reusability and Regeneration Study

In Figure 9, the results from the regeneration and reusability study of the adsorbent are given after five successive cycles of adsorption and desorption. Initially, the %R after adsorption was relatively high, about 95—100% in the first cycle. This high %R shows a strong affinity and the presence of more active sites on the surface of the adsorbent. A slight decline was observed across each cycle, resulting in about 60% to 65% by the end of the fifth cycle, which is attributed to a minimum saturation of the adsorption sites and incomplete desorption of RY-84 dye molecules that may likely disrupt further adsorption. During the desorption study, the composite maintained a high removal efficiency from 85% to 95% across the cycles of regeneration. The consistent %R of the adsorbent indicates its rigid nature and the ability to endure chemical alterations when adsorption and desorption were repeatedly done. The robustness of the desorption study implies that only physical interaction occurred between RY-84 molecules and the composite, resulting in easy regeneration void of any loss on the surface functionality of the adsorbent, and the reusability behaviors indicate the stable and durable nature of the material. After five successive cycles, 60% of the adsorbent's initial adsorption capacity was retained, making it more suitable for multiple usages in wastewater purification. This excellent reusable feature is derived from the interaction between the nanoparticles and reduced graphene oxide because the matrix of the rGO provides a large surface area that is specific for this interaction, thereby facilitating the adsorption efficiency and providing stability for regeneration. The nanocomposite in this case appears more stable and effective, can regenerate adsorbent, and is ideal for treating dye-contaminated wastewater.

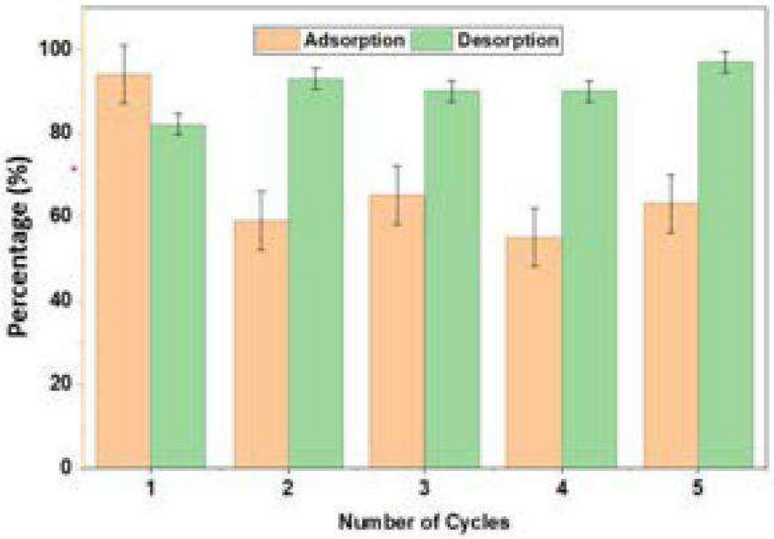

Figure 9. Regeneration and reusability study of Ag-rGO NC for RY-84 adsorption from aqueous solution

Adsorption isotherm and kinetics studies

The surface properties, adsorption mechanisms, and interaction energies between the composite and RY-84 dye molecules were studied. Three widely used isotherms were employed to assessed the equilibrium of adsorption of the dye onto the composite. These includes, Langmuir, Freundlich and Temkin isotherms (Fig. 10) and the corresponding table contains summary of the parameters for each model (Table 1). In Equation 5, the linear form the Langmuir isotherm is presented.

$$\frac{Ce}{qe} = \frac{Ce}{qm} + \frac{1}{q_m K_L} \quad (5)$$

In the above equation, Ce is the adsorption capacity at equilibrium, the maximum adsorption capacity is represented by qm, and KL is the Langmuir constant. The plot of Ce/Qe versus Ce was constructed and given in Figure 10a. An excellent correlation was obtained, indicating the occurrence of monolayer adsorption on a homogeneous surface with a small number of similar sites for binding. There is a high affinity between the dye molecules and the active sites of the composite, evidenced by the Langmuir constant (KL = 0.02774 L/mg) and maximum adsorption capacity (Qmax = 70.5821 mg/g), respectively. The nature of the adsorption process is favorable and spontaneous from the dimensionless separation factor (RL = 0.42575), which is between 0 and 1. The dye exhibits Langmuir-type behavior after being anchored on the composite under the study's conditions, indicating a uniformed monolayer coverage of the dye's molecules after being formed across the surface of the adsorbent [61].

Conversely, with an R^2 value of 0.926, the Freundlich isotherm—which suggests multilayer adsorption on heterogeneous surfaces—also offered a fair fit to the actual data (Fig. 10b), which is given in its linear form as:

$$log\ q_e = log\ K_F + \frac{1}{n} log\ C_e \quad (6)$$

The amount of dye adsorbed is represented by qe per unit mass of adsorbent given in Equation 6. Ce is the concentration at equilibrium of the dye within the bulk solution, while KF is the Freundlich constant (mg/g) that denotes the adsorption capacity. The intensity of the adsorption in the Freundlich equation is given as n (g/L) and aligns with adsorbate-adsorbent interactions. The heterogeneity factor (1/n) and Freundlich constant (KF) indicate the favorable nature of the adsorption at ($0 < 1/n < 1$) taking place on the surface with non-uniform energized sites [62]. A pi-pi stacking was observed between the aromatic rings of the dye via weak van der Waals forces on the rGO sheets and electrostatic attraction between the negatively charged RY-84 dye anions and positively charged sites of Ag NPS. The adsorption procedure is not limited to a single layer per the Freundlich

model, and the dye molecules might interact with several binding sites. The Ag-decorated nanocomposites display this heterogeneity because changes on the surface add several active sites with different active sites for RY-84 dye molecules [60, 61].

The delineation of adsorption by the Temkin model on the heterogeneous surface of the adsorbent is based on two major assumptions: (1) it provides information on how adsorbates and adsorbents interact and the heat of adsorption, which implies that the heat of adsorption increases as surface coverage increases. (2) It assumes that adsorption takes place on binding sites that are uniformly dispersed with a similar level of energy to a certain point. In Equation 7, the linearized version of the Temkin model is presented.

$$q_e = B \ln A + B \ln C_e \quad (7)$$

Which can also be expressed in equation 8 as :

$$q_e = B \log A + B \log C_e \quad (8)$$

Where, B = RT/b, where "b" is the Temkin constant. In figure 10c, a straight line was obtained when qe vs. ln Ce was plotted. The constants for Eq. (8) were calculated and presented in Table 2.

A strong correlation exists from the Temkin isotherm, indicating the significance of the interactions between the adsorbate and adsorbent during the adsorption process. There is a decline in the heat of adsorption linearly as the surface coverage increases, represented by the Temkin constant (BT = 12.28 J/mol). This suggests a moderate interaction between the active sites on the composite and dye molecules. This behavior suggests that the saturation or repulsive forces trigger the energy required to further reduce adsorption as the material's surface becomes saturated. The Temkin binding equilibrium constant (KT = 0.2147 L/mg) confirms favorable adsorption consistent with chemisorptive interactions, such as coordination between the NPs and functional groups of the dye, with similar scenarios already reported in the literature [63, 64]. The various isothermal findings suggest that the surface of the composite experienced both monolayer and multilayer adsorption simultaneously. The Freundlich and Temkin isotherms display multilayer adsorption and interaction effects with increased surface coverage, while the strong Langmuir fit depicts the initial dominance of monolayer adsorption at low dye concentrations from the heterogeneous surface of the composite where physical adsorption occurred and was enhanced via π-conjugated extension, pi-pi stacking, and electrostatic interactions following the availability of active adsorption sites on the nanoparticles, leading to chemisorption.

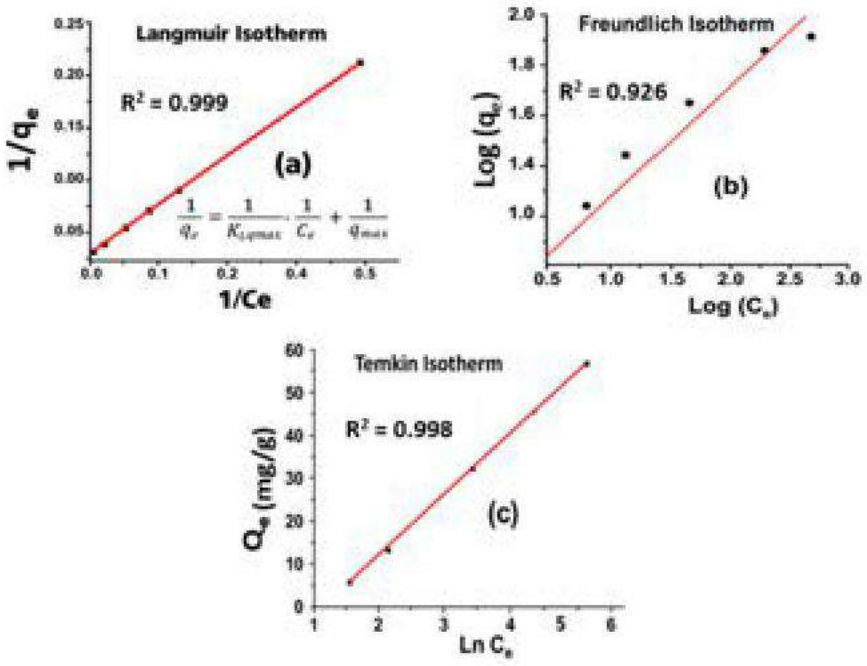

Figure 10. Adsorption isotherms fitting for RY-84 removal on Ag-rGO NC, (a) Langmuir, (b) Freundlich, and (c) Temkin models

Table 1. Summary table for Parameters of Various Adsorption Isotherm Models for RY-84 Dye removal onto Ag–rGO NC

Langmuir Isotherm	Adsorbent	Intercept	Slope	Q_{max} (mg/g)	K_L	R_L	R^2
	Ag-rGO	0.12664	0.4462	70.5821	0.02774	0.42575	0.999
Freundlich Isotherm	**Ag-rGO**	**Intercept**	**Slope**	**1/n**	**k_f**	**R^2**	
		0.55726	0.53009	0.53009	4.4497852	0.926	
Temkin Isotherm	**Ag-rGO**	**B_T (J mol^{-1})**	**K_F (L.mg^{-1})**	**R^2**			
		12.28	0.2147	0. 998			

Kinetics Study of RY-84 dye removal onto Ag-rGO

The mechanism and rate-determining steps in RY-84 dye adsorption on the adsorbent and the kinetic studies were done using pseudo-first-order and pseudo-second-order kinetic models. The difference in the adsorption rate as a function of time was described using these models to further determine whether the process was dominated by either physical or chemical interactions. The linear form of the pseudo-first-order model is given in Equation (9) [52]:

$$log\ (q_e - q_t) = log\ q_e - \frac{k1t}{2.303} \quad (9)$$

Where qe (mg g^{-1}) and qt (mg g^{-1}) represent the amounts of RY-84 dye adsorbed at equilibrium and at time t (min), respectively, while k1 (min^{-1}) is the rate constant for the pseudo-first-order reaction. The value of k1 is obtained from the slope of the linear plot of log (qe−qt) versus time, which characterizes the adsorption rate under this kinetic assumption (Figure 11a). The pseud-second-order kinetic model, which assumes that chemisorption is the rate-limiting step involving valence forces through sharing or exchange of electrons between adsorbent and adsorbate, is represented in its linear form as shown in Equation (10):

$$1/q_t = 1/k_2 q_e^2 + t/q_e \quad (10)$$

Where, k2 (g mg^{-1} min^{-1}) denotes the pseudo-second-order rate constant, while qe and qt represent the quantity of RY-84 dye attached before reaching equilibrium. The parameters k2 and qe are calculated from the slope and intercept of the linear plot of t/qt versus t (Figure 11b). Fitted kinetic plots for both models are given in (Figure 11), and the derived parameters are summarized in (Table 2).

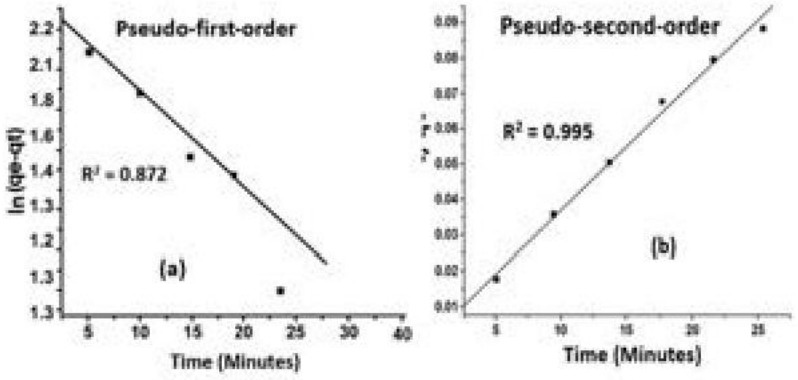

Figure 11. Kinetics plots of RY-84 Dye adsorption on Ag-rGO NC, (a) pseudo-first-order model, and (b) pseudo-second-order model.

From the kinetic data, the equilibrium adsorption capacity (qe) value is given as 55.321 mg g^{-1}; k_1, which is the rate constant, is 0.067 min^{-1}, while the correlation coefficient (R^2) is 0.872. The q_e value for pseudo-second-order is 41.63 mg g^{-1} with a rate constant (k_2) recorded as 0.005 min^{-1}. The pseudo-second-order (R2 = 0.995) model is much higher compared to the pseudo--first-order (R2 = 0.872) (Table 2). This high R^2 value suggests that the ideal kinetic model for the adsorption process is pseudo-second-order, and the adsorption process is specifically driven by the mechanisms of chemisorption. Chemical interactions between functional groups on the adsorbent's surface and RY-84 dye molecules include complexation and sharing of electrons. These interactions further indicate that the adsorption of the adsorbate was influenced by chemical bonding and surface reactions other than diffusion. The rate constant (k_2) value is moderate, suggesting that the rate of adsorption is governed by intra--particle diffusion and equilibrium time despite being chemically influenced. The derived qe value (41.63 mg g^{-1}) implies that high affinity influenced the composite toward RY-84 dye molecules. This is due to the synergistic effect occurring between the nanoparticles and rGO, generating a large surface area, abundant active sites, and improved electrical conductivity, yielding strong interactions between the composite and the dye molecules. The pseudo-first-order and pseudo-second-order data indicate that diffusion and reaction mechanisms on the surface of the adsorbent influenced the adsorption of the dye, with chemisorption being the most dominant reaction, which is consistent with previous findings on the use of nanocomposites for dye removal [52].

Table 2. Summary of kinetic parameters for RY-84 adsorption on Ag-rGO NC

Adsorbent	**Pseudo-first-order**			
	Co (mg/l)	q_e (mg/g)	k_1 (min^{-1})	R^2
Ag-rGO NC	10	55.321	0.067	0.872
	Pseudo-second-order			
	10	q_e (mg/g)	k_2 (g/mg.min)	R^2
		41.63	0.005	0.995

Thermodynamic Study

Findings from the thermodynamic studies on RY-84 adsorption are presented in (Table 3). The equilibrium constant (Kc) decreased from 206 (303 K) to 10 (333 K). This implies that at higher temperatures, the rates of adsorption declined. This observation further implies that the process was exothermic because as temperature increased, desorption of the RY-84 molecules is likely to occur on the surface of the Nano composite. The negative values for the Gibbs free energy confirm that the adsorption process was spontaneous for the different temperature ranges. Howbeit, the decline in the ΔG° with temperatures indicates that the spontaneous nature of the process decreased when the temperature increased, implying the exothermic nature of the process. The derived values for enthalpy (ΔH°) and entropy (ΔS°) were obtained from the van't Hoff plot (ln Kc versus 1/T, R^2 = 0.956), which presents essential mechanistic clarifications (Figure12). More energy was required to enhance the adsorption process, evidenced by the positive value of ΔH°, perhaps due to surface activation and interaction between the surfaces of the adsorbent and the absorbate. Physisorption is the dominant mechanism observed during the process due to the exothermic nature related to high temperatures but with likely contributions from weak chemical interactions between RY-84 molecules and functional groups on the adsorbent's surface.

Table 3. Thermodynamic Parameters for RY-84 adsorption on Ag-rGO NC surface

T (K)	C_e (mg/L)	K_c	ΔG° (kj/mol)	ΔS° (J/mol)	ΔH° kJ/mol K
303	1.54	206	-15.47	-231.5	69.82
313	1.87	112	-13.39		
323	2.62	33.4	-9.26		
333	6.51	10	-7.78		

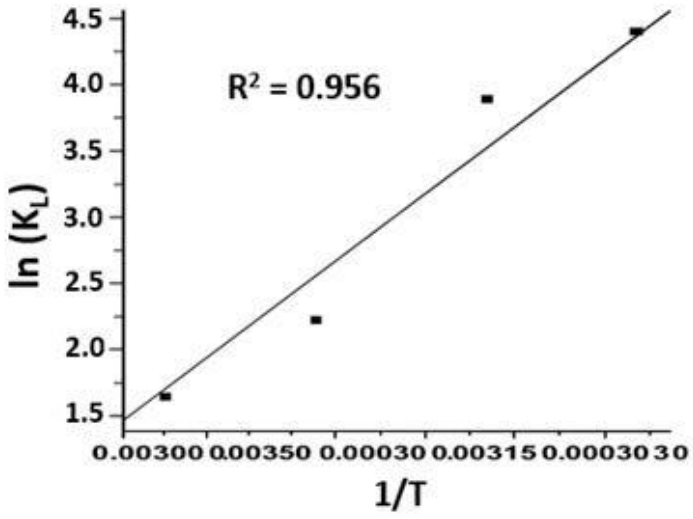

Figure 12. Van't Hoff plot of RY-84 Dye Adsorption on Ag-rGO NC.

Conclusion

Green-synthesized Ag NPs decorated on rGO nanocomposite proved effective for RY-84 dye adsorption from wastewater. The adsorption behavior of the adsorbent highlights the importance of green chemistry principles for the synthesis of eco-friendly materials for wastewater treatment. The utilization of DCW as a reducing and stabilizing agent provides a novel approach for producing environmentally friendly and cost-effective nanocomposites with enhanced adsorption efficiency, surface reactivity,

and improved structural stability. Results from the comparative studies of chemical and biologically synthesized graphene materials offer new insight on the impact of their adsorption performance, synthesis pathways, and surface functionality. The nanocomposites exhibited various essential characteristics, such as ease of regeneration and high and consistent adsorption performance, stressing the need for scale-up in wastewater treatment. This study, however, establishes a firm scientific basis for the future design of biologically synthesized hybrid nanomaterials that is environmentally sustainable with high adsorption performance.

Declaration of competing interest

The authors state that none of the work described in this study could have been influenced by any known competing financial interests or personal relationships.

References

1. Alam S, Khan MS, Umar A, Khattak R, Zekker I, et al. (2021) Preparation of Pd–Ni nanoparticles supported on activated carbon for efficient removal of basic blue 3 from water. Water, 13: 1211.

2. Mahar I, Mahar FK, Mahar N, Memon AA, Pirzado AAA, et al. (2023) Fabrication and characterization of MXene/carbon composite-based nanofibers (MXene/CNFs) membrane: An efficient adsorbent material for removal of Pb+2 and As+3 ions from water. Chemical Engineering Research and Design, 191: 462-471.

3. Njewa JB, Shikuku VO (2023) Recent advances and issues in the application of activated carbon for water treatment in Africa: A systematic review (2007–2022). Applied Surface Science Advances, 18: 100501.

4. Lee B, Kim C (2024) Innovative membrane technology for water treatment solutions: Current status and future prospects of carbon nanotube membranes. Environmental Engineering Research, 29.

5. Xie Y, Zhang T, Wang B, Wang W (2024) The application of metal–organic frameworks in water treatment and their large-scale preparation: A review. Materials, 17: 1972.

6. Seah MQ, Chua SF, Ang WL, Lau WJ, Mansourizadeh A, et al. (2024) Advancements in polymeric membranes for challenging water filtration environments: A comprehensive review. Journal of Environmental Chemical Engineering, 12: 112628.

7. Shahzad MK, Memon FH, Soomro F, Iqbal M, Ibrar A, et al. (2023) MoS2-based lamellar membranes for mass transport applications: Challenges and opportunities. Journal of Environmental Chemical Engineering, 11: 109329.

8. Mangalam J, Kumar M, Sharma M, Joshi M (2019) High adsorptivity and visible light assisted photocatalytic activity of silver/reduced graphene oxide (Ag/rGO) nanocomposite for wastewater treatment. Nano-Structures & Nano-Objects, 17: 58-66.

9. George D, James G, Manjally JK, Thomas J, Kuriakose MS, et al. (2020) Graphene/PANI electrode material characterization for supercapacitor application. Materials Today: Proceedings, 24: 1734-1741.

10. Trikkaliotis DG, Mitropoulos AC, Kyzas GZ (2020) Low-cost route for top-down synthesis of over-and low-oxidized graphene oxide. Colloids and Surfaces A: Physicochemical and Engineering Aspects, 600: 124928.

11. Yu X, Zhang W, Zhang P, Su Z (2017) Fabrication technologies and sensing applications of graphene-based composite films: Advances and challenges. Biosensors and Bioelectronics, 89: 72-84.

12. Abu-Nada A, Abdala A, McKay G (2021) Removal of phenols and dyes from aqueous solutions using graphene and graphene composite adsorption: A review. Journal of Environmental Chemical Engineering, 9: 105858.

13. Malik A, Khan A, Anwar N, Naeem M (2020) A comparative study of the adsorption of Congo red dye on rice husk, rice husk char and chemically modified rice husk char from aqueous media. Bulletin of the Chemical Society of Ethiopia, 34: 41-54.

14. Mehra S, Singh M, Chadha PJ (2021) Adverse impact of textile dyes on the aquatic environment as well as on human beings. Toxicology International, 28: 165.

15. Ji J, Yuan X, Zhao Y, Jiang L, Wang H (2022) Mechanistic insights of removing pollutant in adsorption and advanced oxidation processes by sludge biochar. Journal of Hazardous Materials, 430: 128375.

16. Nasrollahzadeh M, Jaleh B, Baran T, Varma RS (2020) Efficient degradation of environmental contaminants using Pd-RGO nanocomposite as a retrievable catalyst. Clean Technologies and Environmental Policy, 22: 325-335.

17. Mondal S, Patel S, Majumder SK (2020) Bio-extract assisted in-situ green synthesis of Ag-RGO nanocomposite film for enhanced naproxen removal. Korean Journal of Chemical Engineering, 37: 274-289.

18. Kamali M, Esmaeili H, Tamjidi S (2022) Synthesis of zeolite clay/Fe-Al hydrotalcite composite as a reusable adsorbent for adsorption/desorption of cationic dyes. Arabian Journal for Science and Engineering, 47: 6651-6665.

19. Siddiqui MF, Khan EA, Alam Khan T (2019) Synthesis of MoO3/polypyrrole nanocomposite and its adsorptive properties toward cadmium (II) and Nile blue from aqueous solution: Equilibrium isotherm and kinetics modeling. Environmental Progress & Sustainable Energy, 38: e13249.

20. Foroutan R, Peighambardoust SJ, Esvandi Z, Khatooni H, Ramavandi B (2021) Evaluation of two cationic dyes removal from aqueous environments using CNT/MgO/CuFe2O4 magnetic composite powder: A comparative study. Journal of Environmental Chemical Engineering, 9: 104752.

21. Sajid M, Sharma A, Choudhry A, Chaudhry SA (2023) Synthesis, characterization and potential application of functionalised binary metallic sulphide for water reclamation. Colloids and Surfaces C: Environmental Aspects, 1: 100011.

22. Alali AF, Almojil SF, Almohana AI, Anqi AE, Rajhi AA, et al. (2023) Hydroxyapatite@Mn–Fe composite as a reusable sorbent for removal of Nile blue dye and Cr (VI) from polluted water. Environmental Science and Pollution Research, 30: 18419-18437.

23. Zhou S, Gao J, Wang S, Fan H, Huang J, et al. (2020) Highly efficient removal of Cr (VI) from water based on graphene oxide incorporated flower-like MoS2 nanocomposite prepared in situ hydrothermal synthesis. Environmental Science and Pollution Research, 27: 13882-13894.

24. Chowdhury A, Khan AA, Kumari S, Hussain S (2019) Superadsorbent Ni–Co–S/SDS nanocomposites for ultrahigh removal of cationic, anionic organic dyes and toxic metal ions: Kinetics, isotherm and adsorption mechanism. ACS Sustainable Chemistry & Engineering, 7: 4165-4176.

25. Abedinpour S, Mahkam M, Zonouz AM (2024) Graphenic molybdenum disulfide nanocomposites as heterogeneous nano--catalyst for reduction of nitroanilines. Journal of Photochemistry and Photobiology A: Chemistry, 448: 115281.

26. Gbawoquiya FL, Rachna K, Narayanan SS, Singh PK, Shankar S, et al. (2024) Facile synthesis and adsorptive removal of Rhodamine B dye from aqueous medium using green synthesized nanocomposite. Zastita Materijala, 65: 452-465.

27. Gbawoquiya FL, Rachna K, Singh PK, Noor IM, Yahya MZA, et al. (2025) Adsorption of cationic basic fuchsin dye from aqueous solution using green synthesized zinc oxide coated on reduced graphene oxide nanocomposite (ZnO-rGO NC). Ionics, 31: 1077-1093.

28. Haldorai Y, Shim JJ (2014) An efficient removal of methyl orange dye from aqueous solution by adsorption onto chitosan/MgO composite: A novel reusable adsorbent. Applied Surface Science, 292: 447-453.

29. Li J, Feng J, Yan W (2013) Synthesis of polypyrrole-modified TiO2 composite adsorbent and its adsorption performance on acid red G. Journal of Applied Polymer Science, 128: 3231-3239.

30. Palmiter RD (1998) The elusive function of metallothioneins. Proceedings of the National Academy of Sciences, 95: 8428-8430.

31. Srikar SK, Giri DD, Pal DB, Mishra PK, Upadhyay SN (2016) Green synthesis of silver nanoparticles: A review. Green and Sustainable Chemistry, 6: 34-56.

32. Nair PP, Beevi S (2023) Impact of nanomaterials on microbial communities: Applications and future perspectives. In: Sustainable Nanomaterials for Biomedical Engineering, 379-413.

33. Jha AK, Prasad K (2019) Nanomaterials from biological and pharmaceutical wastes – A step towards environmental protection. Materials Today: Proceedings, 18: 1465-1471.

34. Li B, Cao H (2011) ZnO@graphene composite with enhanced performance for the removal of dye from water. Journal of Materials Chemistry, 21: 3346-3349.

35. Jayachandiran J, Ponnusamy M, Muthukrishnan P, Sundaram M, Jeyaprakash BG (2018) Synthesis and electrochemical studies of rGO/ZnO nanocomposite for supercapacitor application. Journal of Inorganic and Organometallic Polymers and Materials, 28: 2046-2055.

36. Hummers WS Jr, Offeman RE (1958) Preparation of graphitic oxide. Journal of the American Chemical Society, 80: 1339.

37. Dreyer DR, Park S, Bielawski CW, Ruoff RS (2010) The chemistry of graphene oxide. Chemical Society Reviews, 39: 228-240.

38. Marcano DC, Kosynkin DV, Berlin JM, Sinitskii A, Sun Z, et al. (2010) Improved synthesis of graphene oxide. ACS Nano, 4: 4806-4814.

39. Pei S, Cheng HM (2012) The reduction of graphene oxide. Carbon, 50: 3210-3228.

40. Stankovich S, Dikin DA, Piner RD, Kohlhaas KA, Kleinhammes A, et al. (2007) Synthesis of graphene-based nanosheets via chemical reduction of exfoliated graphite oxide. Carbon, 45: 1558-1565.

41. Dikin DA, Stankovich S, Zimney EJ, Piner RD, Dommett GHB, et al. (2007) Preparation and characterization of graphene oxide paper. Nature, 448: 457-460.

42. Fernández-Merino MJ, Guardia L, Paredes JI, Villar-Rodil S, Solís-Fernández P, et al. (2010) Vitamin C is an ideal substitute for hydrazine in the reduction of graphene oxide suspensions. The Journal of Physical Chemistry C, 114: 6426-6432.

43. Zhu Y, Murali S, Cai W, Li X, Suk JW, et al. (2010) Graphene and graphene oxide: Synthesis, properties, and applications. Advanced Materials, 22: 3906-3924.

44. Sreeprasad TS, Maliyekkal SM, Lisha KP, Pradeep T (2013) Reduced graphene oxide–silver nanocomposite as an efficient scavenger of mercury. Journal of Hazardous Materials, 186: 921-931.

45. Liu S, Tian J, Wang L, Luo Y, Sun X, et al. (2011) Self-assembled graphene platelet–glucose oxidase nanostructures for glucose biosensing. Biosensors and Bioelectronics, 26: 4491-4496.

46. Zhang H, Lv X, Li Y, Wang Y, Li J (2010) P25-graphene composite as a high-performance photocatalyst. ACS Nano, 4:

380-386.

47. Tang L, Wang Y, Li Y, Feng H, Lu J, et al. (2013) Preparation, structure, and electrochemical properties of reduced graphene sheet films. Advanced Functional Materials, 19: 2782-2789.

48. Kaliraj L, Ahn JC, Rupa EJ, Abid S, Lu J, et al. (2019) Synthesis of panos extract mediated ZnO nano-flowers as photocatalyst for industrial dye degradation by UV illumination. Journal of Photochemistry and Photobiology B: Biology, 199: 111588.

49. Iravani S (2011) Green synthesis of metal nanoparticles using plants. Green Chemistry, 13: 2638-2650.

50. Song JY, Kim BS (2009) Rapid biological synthesis of silver nanoparticles using plant leaf extracts. Bioprocess and Biosystems Engineering, 32: 79-84.

51. Sun Y, Mayers B, Herricks T, Xia Y (2003) Polyol synthesis of uniform silver nanowires: A plausible growth mechanism and the supporting evidence. Nano Letters, 3: 955-960.

52. Park S, Ruoff RS (2009) Chemical methods for the production of graphenes. Nature Nanotechnology, 4: 217-224.

53. Zhu Y, Murali S, Cai W, Li X, Suk JW, et al. (2010) Graphene and graphene oxide: Synthesis, properties, and applications. Advanced Materials, 22: 3906-3924.

54. Compton OC, Nguyen ST (2010) Graphene oxide, highly reduced graphene oxide, and graphene: Versatile building blocks for carbon-based materials. Small, 6: 711-723.

55. Ali MH, Goher ME, Al-Afify AD, El-Sayed SM (2022) A facile method for synthesis rGO/Ag nanocomposite and its uses for enhancing photocatalytic degradation of Congo red dye. SN Applied Sciences, 4: 276.

56. Ahmad H, Albaqawi HS, Yusoff N, Reduan SA, Yi CW (2020) Reduced graphene oxide-silver nanoparticles for optical pulse generation in ytterbium- and erbium-doped fiber lasers. Scientific Reports, 10: 9408.

57. Malard LM, Pimenta MA, Dresselhaus G, Dresselhaus MS (2009) Raman spectroscopy in graphene. Physics Reports, 473: 51-87.

58. Ju J, Liu W, Perlaki CM, Chen K, Feng C, et al. (2017) Sustained and cost effective silver substrate for surface enhanced Raman spectroscopy based biosensing. Scientific Reports, 7: 6917.

59. Fan Z, Li J, Li P, Ye Q, Xu H, et al. (2017) Protein arginine methyltransferase 1 (PRMT1) represses MHC II transcription in macrophages by methylating CIITA. Scientific Reports, 7: 40531.

60. Natasha, Khan A, Rahman UU, Sadaf, Yaseen M, et al. (2024) Effective removal of Nile blue dye from wastewater using silver-decorated reduced graphene oxide. ACS Omega, 9: 19461-19480.

61. Brinza L, Maftei AE, Tascu S, Brinza F, Neamtu M (2022) Advanced removal of Reactive Yellow 84 azo dye using functionalised amorphous calcium carbonates as adsorbent. Scientific Reports, 12.

62. Nadafi K, Vosoughi M, Asadi A, Borna MO, Shirmardi M (2014) Reactive Red 120 dye removal from aqueous solution by adsorption on nano-alumina. Journal of Water Chemistry and Technology, 36: 125-133.

63. Singh KP, Wareppam B, Raghavendra KG, Singh NJ, de Oliveira AC, et al. (2023) Heterophase grain boundary-rich super-

paramagnetic iron oxides/carbon composite for cationic crystal violet and anionic Congo red dye removal. Advanced Engineering Materials, 25: 2300354.

64. Priya VS, Basha SK, Kumari VS (2023) Kinetics and adsorption performance of biosorbent starch/poly(vinyl alcohol)/-graphene oxide nanocomposite for the removal of dyes. Journal of Umm Al-Qura University for Applied Sciences, 9: 529-547.